remote sensing

MDPI

Article

Accessible Remote Sensing Data Mining Based Dew Estimation

Ying Suo [1], Zhongjing Wang [1,2,*], Zixiong Zhang [1] and Steven R. Fassnacht [3,4,5]

[1] Department of Hydraulic Engineering, Tsinghua University, Beijing 100084, China
[2] State Key Lab (Breeding Base) of Land Degradation and Ecological Restoration in Northwest China, Ningxia University, Yinchuan 750021, China
[3] ESS-Watershed Science, Colorado State University, Fort Collins, CO 80523-1476, USA
[4] Cooperative Institute for Research in the Atmosphere, Colorado State University, Fort Collins, CO 80523-1375, USA
[5] Natural Resources Ecology Lab, Colorado State University, Fort Collins, CO 80523-1499, USA
* Correspondence: zj.wang@tsinghua.edu.cn

Abstract: Dew has been considered a supplementary water resource as it constitutes an important water supply in many ecosystems, especially in arid and semiarid areas. Remote sensing allows large-scale surface observations, offering the possibility to estimate dew in such arid and semiarid regions. In this study, by screening and combining different remote sensing variables, we obtained a well-performing monthly scale dew yield estimation model based on the support vector machine (SVM) learning method. Using daytime and nighttime land surface temperatures (LST), the normalized difference vegetation index (NDVI), and three emissivity bands (3.929–3.989 μm, 10.780–11.280 μm, and 11.770–12.270 μm) as the model inputs, the simulated site-scale monthly dew yield achieved a correlation coefficient (CC) of 0.89 and a root mean square error (RMSE) of 0.30 (mm) for the training set, and CC = 0.59 and RMSE = 0.55 (mm) for the test set. Applying the model to the Heihe River Basin (HRB), the results showed that the annual dew yield ranged from 8.83 to 20.28 mm/year, accounting for 2.12 to 66.88% of the total precipitation, with 74.81% of the area having an annual dew amount of 16 to 19 mm/year. We expanded the model application to Northwest China and obtained a dew yield of 5~30 mm/year from 2011 to 2020, indicating that dew is a non-negligible part of the water balance in this arid area. As a non-negligible part of the water cycle, the use of remote sensing to estimate dew can provide better support for future water resource assessment and analysis.

Keywords: dew estimation; machine learning; remote sensing; Northwest China

Citation: Suo, Y.; Wang, Z.; Zhang, Z.; Fassnacht, S.R. Accessible Remote Sensing Data Mining Based Dew Estimation. *Remote Sens.* **2022**, *14*, 5653. https://doi.org/10.3390/rs14225653

Academic Editor: Gilles Boulet

Received: 12 September 2022
Accepted: 4 November 2022
Published: 9 November 2022

1. Introduction

Dew, including water vapor adsorption and dew deposition, is a frequent and natural phenomenon [1]. It is hypothesized that studies regarding dew, both observations and studies regarding its utilization, began in ancient times [2]. The historical record of dew capture for the water demand dates back to the early Greeks in 600 B.C. [3]. In recent years, dew has been considered a valuable water source in arid and semiarid areas [4] for plant growth [5], biotic crust processes [6], and the survival of desert arthropods [7].

Dew was identified as a part of the water balance [8], but this was not initially well recognized. In recent years, the significance of dew in the water balance has been recognized with the development of dew measurement techniques and estimation methodologies [9–11]. Direct dew measurement techniques include the radiative dew condenser (RDC) [12,13], the micro/mini lysimeter (ML) [14], the Hiltner dew balance (HDB) [15], and the cloth-plate method (CPM) [16]. Among these, the RDC condensation surface is a man-made material mainly used for dew water collection studies [17]. MLs can represent dew's natural form and condition, but their size, composition, and other parameters produce substantial uncertainty among the results [18]. The HDB and CPM condensation surfaces are metal and glass, respectively, rather than soil, thus soil water vapor adsorption, an

important component of dew water in arid and semiarid areas [1], cannot be observed using these methods.

The dew estimation method is mainly based on energy balance by calculating the negative nighttime latent heat, i.e., the downward water vapor flux, which is converted to dew yield [19]. The estimation methods typically uses the Penman–Monteith equation (PM) [20], or eddy covariance (EC) [21,22]. The EC method is the first direct observation of water vapor change by measuring the pulsation of vertical wind speed and water vapor density, which has fewer theoretical assumptions and higher accuracy than the PM method. The EC method is considered the standard in daytime latent heat flux, i.e., evapotranspiration, and observation in the field [23]. Since observations made using the EC method can be automated and compared with manual measurement methods such as CPM and HDB, they can be used for long-term continuous monitoring. However, there is no unified method for dew observation [13,18,22] or quantification, especially for large-scale dew estimation. Such methods should be further developed [11,19,24].

Remote sensing data provides input to the large-scale estimation of many hydrological variables, such as evapotranspiration (ET) [25], soil moisture [26], and precipitation [27]. Some studies attempted to estimate large-scale dew, for example, by using the Soil Moisture Experiments 2005 (SMEX05) data [28] and meteorological reanalysis data [29]. However, in areas lacking meteorological observations, the development of estimation methods directly based on remote sensing data is a solution to the problem of large-scale dew estimation.

Machine learning provides intelligent methods by which to estimate hydrological parameters from remotely sensed data [30]; it has also been applied to dew estimation. support vector machine (SVM) is a machine-learning algorithm proposed by Shalev-Shwartz, et al. [31] and has been widely used for classification, regression, and other learning tasks [32]. In particular, LIBSVM, a type of SVM software proposed in 2011 [32], has been well applied in potential evapotranspiration (ET) (latent heat flux) estimation [25]; it was mainly used in this study to estimate dew, also known as negative latent heat flux.

In arid and semiarid regions, it is of great interest to assess the amount of dew water from the atmosphere. The main objective of this study was to develop and evaluate an SVM model to (1) analyze the performance of simulated dew under different variables to filter the optimal combination; (2) access the performance of the SVM method for different underlying surface conditions; (3) estimate the dew yield in the study area by remote sensing data; and (4) analyze the possible association with and relative contribution of each remote sensing factor to dew estimation.

2. Materials and Methods

2.1. Study Area

The Heihe River Basin (HRB) is the second largest endorheic river basin in China (37.7°–42.7°N, 97.1°–102.0°E), covering a catchment area of approximately 143,200 km^2 (Figure 1). The basin has a distinctly cold and arid landscape characterized by snow/glaciers, permafrost, alpine meadows, forests, grasslands, rivers, irrigated crops, riparian ecosystems, the Gobi Desert, and deserts extending from upstream to downstream regions. The upper reaches are in the Qilian Mountains with the snow line at a height of about 4200 m. Over 90% of the population, grain production, and major industries are concentrated in the midstream area [33], and this area consumes large amounts of water via a relatively complete agricultural irrigation system. In the downstream area, the landscape consists of sandy and gravelly deserts; natural oases dominated by *Populus euphratica*, *Tamarix*, and other arid species; and lakes that serve as the terminus of the HRB. The mean annual air temperatures are 0.4 °C, 7.3 °C, and 8.2 °C from the upstream region at an altitude of 2000–5000 m, the midstream region at an altitude of 1000–3000 m, to the downstream region at an altitude of 800–1700 m. The annual precipitation decreased from 322 mm/year and 130 mm/year to 30 mm/year, while the evaporation increased from 954 mm/year and 1324 mm/year to 2248 mm/year in the three reaches, respectively [34].

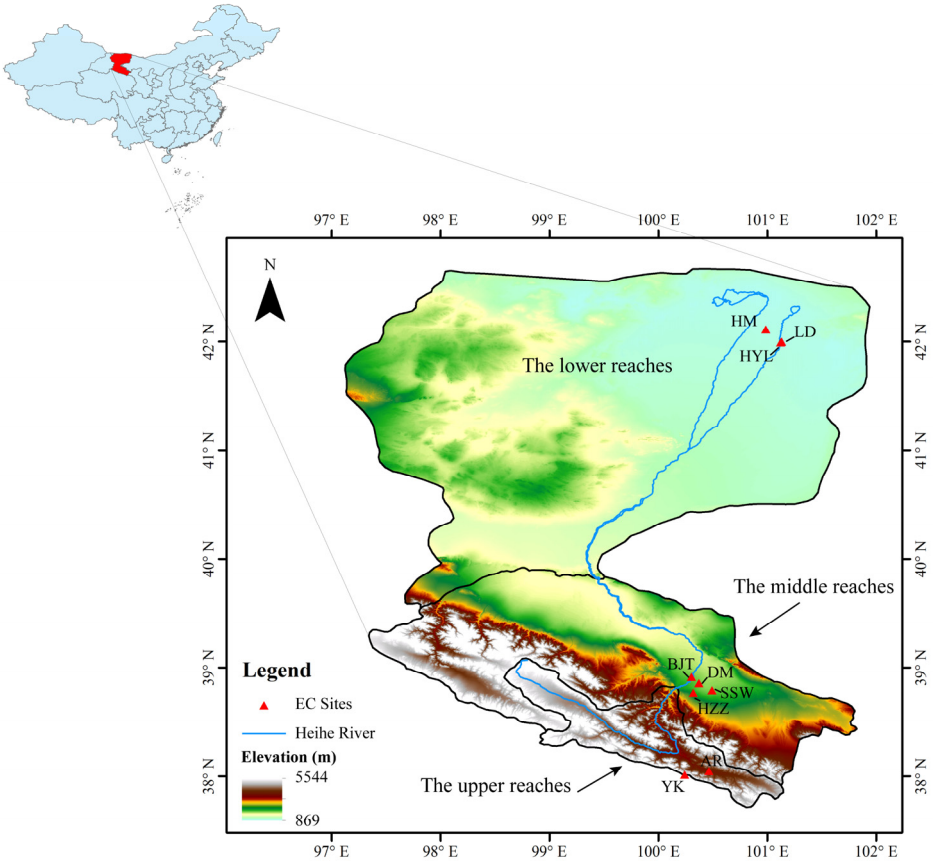

Figure 1. Location of the flux tower sites and topography of the Heihe River Basin.

2.2. Data Source

2.2.1. Eddy-Covariance Data

There are nine eco-hydrological observation stations (flux towers) in the study basin [35–37] located in the upper, middle, and lower reaches of the HRB, respectively. The underlying areas and locations of these stations are shown in Figure 1 and Table 1.

Table 1. EC site information in the Heihe River Basin.

Station	Lon	Lat	Elevation (m)	Observation Period	Landscapes
AR	100.4643	38.0473	3033	January 2013–December 2017	Alpine grassland
HYL	101.1236	41.9928	876	January 2014–December 2015	*P. euphratica*
YK	100.2421	38.0142	4148	September 2015–December 2017	Alpine tundra
LD	101.1326	41.9993	878	January 2014–December 2015	Barren-land
HZZ	100.3201	38.7659	1731	June 2015–December 2017	Desert
SSW	100.4933	38.7892	1594	January 2013–April 2015	Desert
BJT	100.3042	38.9150	1562	January 2013–December 2014	Desert
HM	100.9872	42.1135	1054	May 2015–December 2017	Desert
DM	100.3722	38.8555	1556	January 2013–December 2017	Maize

Each flux observation tower has a three-dimensional sonic anemometer (CSAT-3, Campbell Scientific) and an open-path infrared gas analyzer (LI-7500, LI−COR). The raw 10 Hz EC data were processed using EddyPro software. All the data are from the dataset of the Heihe Integrated Observatory Network (http://heihe.westgis.ac.cn/, accessed on 18 September 2018). The data were processed using spike detection, lag correction, coordinate rotation, sonic virtual temperature correction, frequency response correction, and density fluctuation [38].

The EC data were averaged over 30 min time intervals. The missing data in the 1.5 h intervals were linearly interpolated. Missing data for more than 1.5 h but less than 24 h were interpolated using the mean diurnal variation method [21]. The negative latent heat flux at night was considered the water vapor adsorption or dewfall appearance, collectively known as dew in previous studies and can be estimated using the following formula [21,22]:

$$D = LE/L, \quad (1)$$

where LE is the amount of dew in the 30 min time intervals (mm), LE is the latent heat flux, and L is the latent heat of water vaporization.

However, the simulation of condensation water estimation at the 30 min scale is poor [24], probably due to the large influence of changes in meteorological elements such as wind speed and cloudiness [39]. However, the dew yield is more related to local water vapor conditions [40], from a water resources perspective. The 30 min data were thereafter cumulated on a monthly basis.

2.2.2. Remote Sensing Data

It has been shown that dew is correlated to the horizontal polarized brightness temperature [41], the air temperature [42], and the leaf area index (LAI) [28]. Therefore, we estimate the monthly dew amount by using the MODIS monthly normalized difference vegetation index (NDVI) (MOD13A3) and land surface temperatures (LST) and emissivity (MOD11C3). The NDVI monthly scale data are the average of the 16-day resolution product MOD13A2 values from that month with a spatial resolution of 1 km; the LST and emissivity monthly scale data are the monthly average of the daily scale data with a spatial resolution of 0.05°, which are resampled to 1 km. Both data sets are from the National Aeronautics and Space Administration (NASA) (https://ladsweb.modaps.eosdis.nasa.gov, accessed on 22 May 2022). The variable descriptions are shown in Table 2.

Table 2. Remote sensing data variables.

Variable Name	Description	Units
NDVI	Normalized Difference Vegetation Index	/
LST_D	Daytime Land Surface Temperature	Kelvin
LST_N	Nighttime Land Surface Temperature	Kelvin
$Emis_{20}$	Band 20 (3.660–3.840 μm) emissivity	/
$Emis_{22}$	Band 22 (3.929–3.989 μm) emissivity	/
$Emis_{23}$	Band 23 (4.020–4.080 μm) emissivity	/
$Emis_{29}$	Band 29 (8.400–8.700 μm) emissivity	/
$Emis_{31}$	Band 31 (10.780–11.280 μm) emissivity	/
$Emis_{32}$	Band 32 (11.770–12.270 μm) emissivity	/

2.3. Methodology

2.3.1. Model Structure

The SVM model maps the sample from the original space to a higher-dimensional feature space through the kernel function. The sample is linearly separable in this feature space [43]. For a given training dataset $(\boldsymbol{x_1}, y_1), (\boldsymbol{x_2}, y_2), \ldots, (\boldsymbol{x_m}, y_m)$, $\boldsymbol{x_i}$ is the 9 remote sensing input variables, as shown in Table 2, and y_i is the target concept of the monthly dew amount. The SVM model aims to learn a regression model shaped as in Equation (2) to allow $f(\boldsymbol{x})$ to be as close as possible to y.

$$f(\boldsymbol{x}) = \boldsymbol{w}^T \boldsymbol{x} + b, \quad (2)$$

where $\boldsymbol{w}$ is the weight vector, and b is the noise. The insensitive loss function proposed by Vapnik [43] is defined as follows:

$$L_{\in}(y, \boldsymbol{x}, f(\boldsymbol{x})) = \begin{cases} 0, & if\ |y - f(\boldsymbol{x})| \leq \in \\ |y - f(\boldsymbol{x})| - \in, & otherwise. \end{cases}, \quad (3)$$

The loss function ignores errors when the difference between the predicted and actual values is smaller than a threshold $\in$, as shown in Figure 2. Those outside the $\in$-insensitive are called support vectors, which contribute to the optimization solution. The generalization of the SVM regression model is optimized by minimizing the generalization error, as shown below.

$$\min_{w,b} \frac{1}{2}\|\boldsymbol{w}\|^2 + C\sum_{i=1}^{m} L_{\in}(y_i, \boldsymbol{x_i}, f(\boldsymbol{x_i})), \quad (4)$$

where $\|\boldsymbol{w}\|$ is the Euclidean norm of the weight vector, and parameter C is the cost of the errors.

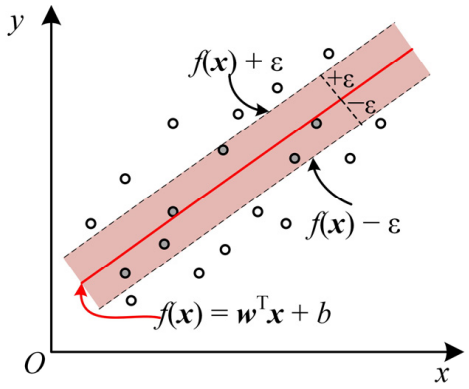

Figure 2. One-dimensional linear regression with an $\in$-insensitive band for the support vector machine (SVM) learning method.

The optimization problem can be solved using Lagrange multipliers. The kernel function $u(\boldsymbol{x}, \boldsymbol{x_i})$ is introduced to bring the training data into a high dimensional feature space. We used the radial basis function (RBF) kernel in this study because previous studies have shown that the RBF kernel performs better than other kernels [44]. The RBF kernel function can be expressed as:

$$u(\boldsymbol{x}, \boldsymbol{x_i}) = \exp\left(-\frac{1}{2\sigma}\|\boldsymbol{x} - \boldsymbol{x_i}\|^2\right), \quad (5)$$

where σ is a variance. Further details of the SVM method can be found in Vapnik [43].

2.3.2. Parametric Optimization Strategy

The SVM model has the following three parameters to be optimized: (1) $\in$, the width of an insensitive error band is set to 0.01; (2) C, the cost of the errors; and (3) σ, the kernel parameters. The proposed parametric optimization strategy consists of four steps (Figure 3). The first step is to initialize the coarse grid search for C (2^{-5}, 2^{-3}, . . . , 2^{5}) and σ (2^{-5}, 2^{-3}, . . . , 2^{5}). The second step is to filter out the model with the test set CC > 0.5 to obtain the range of parameter values. The third step is to detail the grid search for C ($2^{\min-2}$, $2^{\min-1.9}$, . . . , $2^{\max+2}$), and σ ($2^{\min-2}$, $2^{\min-1.9}$, . . . , $2^{\max+2}$). Finally, the optimal models with different combinations of input variables are filtered using the test set CC from highest to lowest. Better performing models can be obtained by secondary grid searching.

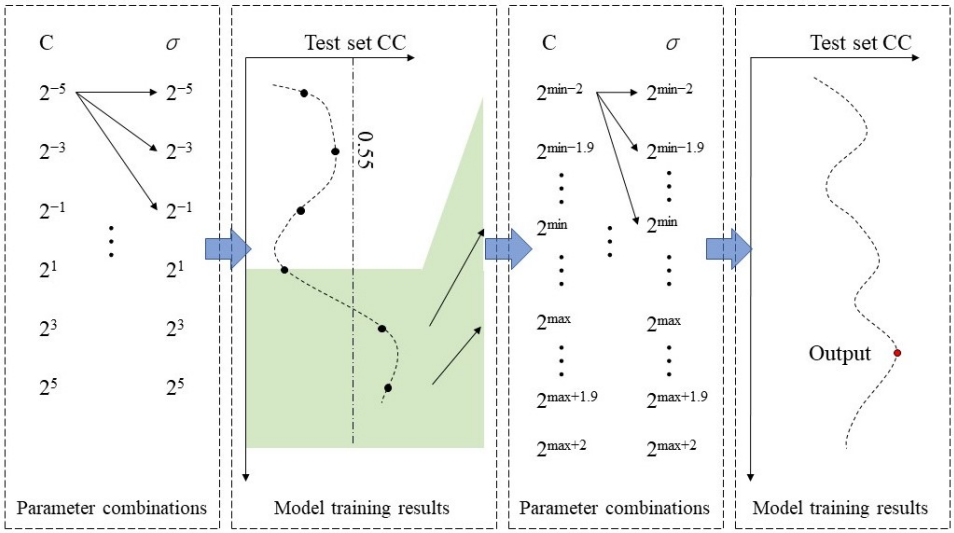

Figure 3. Double-grid search parameter optimization strategy.

In order to reduce the uncertainty, five-fold cross-validation was employed in all the model training processes. All the data were stratified into five groups, each containing ca. 20% of the data. The SVM training was performed five times on four of the groups, and the remaining group was tested. The mean value of the statistical index of the five training results was taken as the performance result of the model under these input and parameter conditions. To avoid a magnitude effect of the input variables, we scaled all the input variables in the range of 0 to 1.

2.3.3. Contribution of Variables

For 'black box' models, determining the contribution of the input variables is important in explaining the model. There are many artificial neural network (ANN)-based methods for calculating the relative contribution degree [45], The connection weights between neurons are the link between inputs and outputs, and the relative contribution of independent variables to the predicted output of a neural network depends primarily on the size and direction of the connection weights [46]. Based on the connection weights of the trained artificial neural network, the contribution of each input variable to the output variable is calculated using Garson's algorithm [47]:

$$RC_i = \frac{\sum_{j=1}^{b}\left(\left|W_{ij}W_{jk}\right|\right)}{\sum_{i=1}^{a}\sum_{j=1}^{b}\left(\left|W_{ij}W_{jk}\right|\right)} \times 100\%, \quad (6)$$

where RC_i is the relative contributions of the ith input to the kth output; W_{ij} is the weight between the ith input and the jth hidden unit; W_{jk} is the weight between the jth hidden unit and the kth output, and k = 1, 2, . . . , c; a, b, c represent the number of neurons in the input, hidden, and output layers of the model, respectively.

To calculate the relative contributions of each input variable, a simple ANN model was built using MATLAB R2019b nftool [48]. We used the default settings, including a two-layer feed-forward network with sigmoid hidden neurons and linear output neurons trained with the Levenberg Marquardt backpropagation algorithm. The hidden layer included 10 neurons, and the output layer included 1 neuron. A total of 70%, 15%, and 15% of the data were randomly selected as the training set, validation set, and test set, respectively; the rest of the parameters had the default values.

2.3.4. Evaluation Criteria

Correlation coefficients (CC) widely used for the evaluation of dew estimation models and for the determination of the correlation of dew with other variables [49,50]. A number of other statistical indicators were also chosen, such as the root mean square error (RMSE), standard deviation (SD), normalized mean bias (NMB), and adjusted R^2 (adj.R^2); see the Equations (7)–(11).

$$CC = \frac{\sum_{i=1}^{n}(D_i - \overline{D})(P_i - \overline{P})}{\sqrt{\sum_{i=1}^{n}(D_i - D_{mean})^2}\sqrt{\sum_{i=1}^{n}(P_i - P_{mean})^2}} \quad (7)$$

$$RMSE = \sqrt{\frac{\sum_{i=1}^{n}(P_i - D_i)^2}{n}}, \quad (8)$$

$$SD = \sqrt{\frac{\sum_{i=1}^{n}(P_i - \overline{P})^2}{n}} \quad (9)$$

$$NMB = \frac{\sum_{i=1}^{n}(P_i - D_i)}{\overline{D}} * 100\% \quad (10)$$

$$\text{adj. } R^2 = 1 - \frac{(1 - R^2)(n-1)}{(n-k-1)} \quad (11)$$

where n is the number of observations; P_i is the dew estimated using machine learning; D_i is the observed dew calculated by Equation (1); $\overline{P}$ is the average of the estimated dew; $\overline{D}$ is the average amount of the observed dew; R^2 is the coefficient of determination; and k is the number of parameters.

The relationship between the RMSE, CC and SD can be described using Taylor diagrams [51], which may assist in evaluating the performance of the models according to the multiple criteria. Taylor diagrams were used to assess the performance of the three best models of different factors, selected from the CCs of the test set, from the highest to the lowest. A Taylor diagram is a polar-style graph that includes the SD of the simulations and the observations, the CC, and the centered RMSE. In a Taylor diagram, the SD is the radial distance from the origin; the cosine of the azimuth angle characterizes the CC; and the RMSE refers to the radial distance from the observed point.

3. Results

3.1. Variable Selection and Contributions

The performances of the optimal models with LST_D and LST_N as fixed variables are given in Table 3. The measurements of the monthly dew yield using the EC method were significantly related to the dew estimates from the models ($p < 0.05$), with the best models achieving the training set and test set CCs of 0.81~0.89 and 0.55~0.64, respectively. None of the models showed significant differences between the training and testing sets, with the difference between the NMB training and testing sets ranging from about −7.4 to 4.4% and the RMSE ranging from about 0.04 to 0.31.

The number of different variables had a significant impact on the simulation results. The overall model performance tended to increase and then decrease with the number of variables increasing. From the performance results of the optimal variable combination model with the different number of variables (m*k*1), the CC and adj.R^2 tended to increase and then decrease with the number of variables. In contrast, the error indicators NMB and RMSE tended to decrease and then increase. The adj.R^2 index can well exclude the influence of the number of variables on the results [52], and the combined performance of the training and testing sets was considered the best simulation effect with 5-7 variables. Treating all the variables as the inputs led to poorer results, suggesting that redundant variables may reduce the simulation effectiveness of the SVM method.

Table 3. The performance with the best combinations of different numbers of input variables under the five-fold cross validation.

Model No.	Variables	Training Set					Test Set				
		CC	NMB	SD	RMSE	adj.R^2	CC	NMB	SD	RMSE	adj.R^2
m31	LST_D, LST_N; $Emis_{31}$	0.73	6.57	0.30	0.49	0.44	0.57	6.27	0.28	0.55	0.23
m32	LST_D, LST_N; $Emis_{32}$	0.66	5.25	0.47	0.50	0.42	0.54	6.53	0.45	0.56	0.20
m33	LST_D, LST_N; $Emis_{23}$	0.62	7.50	0.40	0.52	0.35	0.51	8.10	0.40	0.58	0.16
m41	LST_D, LST_N; $Emis_{23}$, $Emis_{31}$	0.76	4.42	0.49	0.43	0.57	0.57	3.95	0.48	0.55	0.23
m42	LST_D, LST_N; NDVI, $Emis_{22}$	0.74	4.28	0.46	0.44	0.53	0.56	5.16	0.44	0.55	0.22
m43	LST_D, LST_N; NDVI, $Emis_{23}$	0.79	4.89	0.48	0.41	0.60	0.55	5.75	0.46	0.57	0.15
m51	LST_D, LST_N; NDVI, $Emis_{29}$, $Emis_{31}$	0.79	3.95	0.50	0.41	0.61	0.62	1.08	0.52	0.52	0.29
m52	LST_D, LST_N; NDVI, $Emis_{29}$, $Emis_{32}$	0.75	4.74	0.48	0.44	0.54	0.59	4.17	0.50	0.55	0.26
m53	LST_D, LST_N; $Emis_{23}$, $Emis_{29}$, $Emis_{31}$	0.81	3.20	0.51	0.39	0.65	0.55	3.00	0.52	0.57	0.16
m61	LST_D, LST_N; NDVI, $Emis_{22}$, $Emis_{29}$, $Emis_{31}$	0.88	3.21	0.53	0.30	0.77	0.64	10.60	0.59	0.61	0.28
m62	LST_D, LST_N; NDVI, $Emis_{22}$, $Emis_{31}$, $Emis_{32}$	0.89	2.00	0.56	0.30	0.78	0.59	−2.44	0.52	0.55	0.23
m63	LST_D, LST_N; NDVI, $Emis_{20}$, $Emis_{23}$, $Emis_{31}$	0.85	3.77	0.53	0.35	0.71	0.59	3.51	0.50	0.55	0.21
m71	LST_D, LST_N; NDVI, $Emis_{20}$, $Emis_{22}$, $Emis_{29}$, $Emis_{31}$	0.91	2.07	0.56	0.27	0.82	0.64	7.61	0.56	0.55	0.25
m72	LST_D, LST_N; NDVI, $Emis_{20}$, $Emis_{23}$, $Emis_{31}$, $Emis_{32}$	0.87	0.70	0.53	0.33	0.74	0.62	1.99	0.61	0.56	0.21
m73	LST_D, LST_N; NDVI, $Emis_{20}$, $Emis_{23}$, $Emis_{29}$, $Emis_{31}$	0.73	5.47	0.52	0.46	0.50	0.57	3.74	0.52	0.56	0.17
m81	LST_D, LST_N; NDVI, $Emis_{20}$, $Emis_{22}$, $Emis_{23}$, $Emis_{29}$, $Emis_{31}$	0.80	4.50	0.51	0.39	0.62	0.61	5.15	0.50	0.53	0.23
m82	LST_D, LST_N; NDVI, $Emis_{22}$, $Emis_{23}$, $Emis_{29}$, $Emis_{31}$, $Emis_{32}$	0.73	5.54	0.49	0.45	0.51	0.59	3.83	0.50	0.56	0.13
m83	LST_D, LST_N; NDVI, $Emis_{20}$, $Emis_{22}$, $Emis_{23}$, $Emis_{31}$, $Emis_{32}$	0.76	5.00	0.50	0.43	0.56	0.55	4.18	0.49	0.57	0.11
m91	ALL	0.67	7.40	0.42	0.50	0.41	0.60	7.46	0.42	0.53	0.21
m92	ALL	0.67	7.14	0.42	0.49	0.41	0.59	7.39	0.41	0.53	0.20
m93	ALL	0.67	7.39	0.42	0.49	0.41	0.60	6.68	0.41	0.54	0.18

The *RC*s of each variable using the ANN model and Equation (6) (see Section 2.3.3) are shown in Table 4. The highest *RC* was $Emis_{31}$, followed by $Emis_{23}$. In Table 3, it can be seen that when the LST_D and LST_N variables were fixed, the first variable added to the optimal SVM model was $Emis_{31}$ (m31), followed by $Emis_{23}$ (m41). For the m53 model with the top three *RC* rankings for the added variables, the training set performed better than m51 and m52, but the validation set performed poorly and there may have been overfitting. For the optimal SVM models with more variables, $Emis_{23}$ was gradually replaced by $Emis_{22}$, $Emis_{29}$, and $Emis_{20}$.

Table 4. Relative contributions (*RC*) of nine inputs to dew estimation.

	$Emis_{31}$	$Emis_{23}$	$Emis_{29}$	LST_N	NDVI	$Emis_{22}$	LST_D	$Emis_{32}$	$Emis_{20}$
Relative contribution	17.54%	11.88%	11.73%	11.37%	11.29%	10.94%	9.46%	9.36%	6.42%

3.2. Model Performance at Site-Scale

All the data collected from the EC sites were taken as the training data; the Taylor diagrams of the simulation results are shown in Figure 4. The standard deviations of all the models ($p < 0.001$) were smaller than the observed values, indicating that the simulated values may not perform well in the simulation of the peak. The CCs of all the models were in the range of 0.5 to 0.9, indicating that the fitting effect was good. Taking the observation point as the center, the closer the better, that is, the lower the centered RMSE value. The closer the distance to the observation point, the better performance of the model, and m61, m62, and m71 models performed better. The m62 model was chosen for the final application.

The simulation results of the optimal combination model with different numbers of variables are shown in Figure 5. The results showed that, with six~seven variables (Figure 5d,e), the simulation results had an obvious distribution along the 1:1 line, and the simulations for all the types of underlying surfaces had a strong correlation. Under the conditions of more or fewer variables, the phenomenon of overestimation of low values and underestimation of high values was observed (Figure 5a–c,f,g).

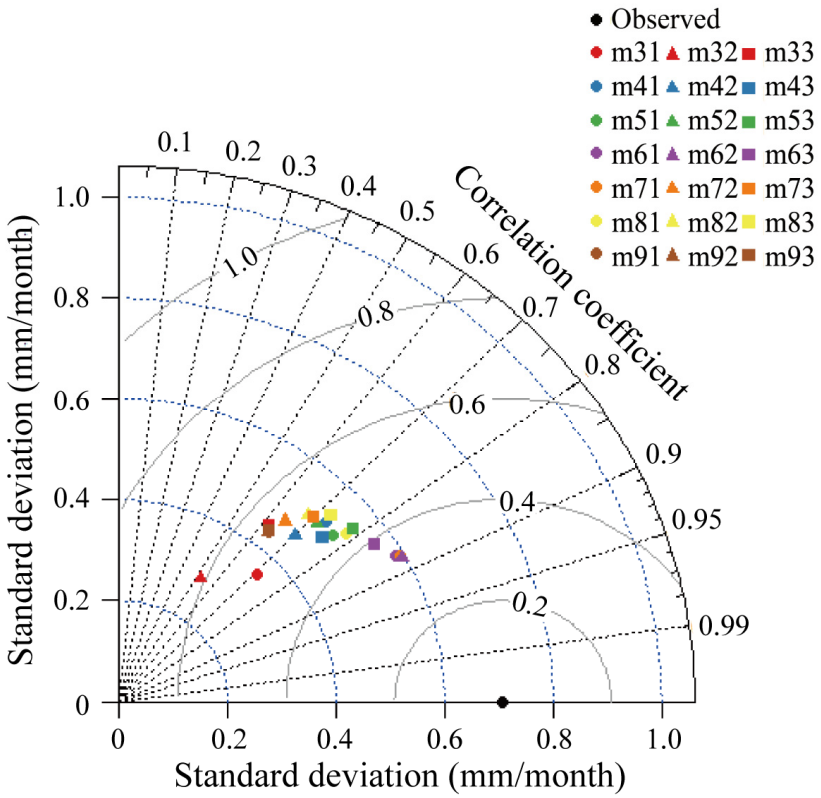

Figure 4. Taylor diagram of all the models.

For the underlying maize, the monthly dew yield may be overestimated with fewer than six variables (Figure 5a–c) or more than eight (Figure 5g). In contrast, underlying alpine tundra and desert may be underestimated with a similar number of variables. The characteristics of the monthly dew yield of *P. euphratica* can be well simulated using 5~7 variables (Figure 5c–e); in other cases, there may be an overestimation of low values and an underestimation of high values. As for underlying bare soil and alpine grassland, 6~7 variables performed better than the other cases (Figure 5d,e).

The m62 model simulated the time series of all the sites' mean results from 2013 to 2017, and the results are shown in Figure 6. The monthly dew yields were reasonably simulated, regardless of whether the overall dew production for the year was high or low. The annual average calculation of the dew yield in each month to obtain the distribution of dew in the year is shown in Figure 7. A clear seasonal distribution of dew yield can be seen. On the EC site scale, the dew yield reached its highest value of 1.81 mm in July, and the average annual dew yield was 15.82 mm/year, which was 24.46% of the total annual precipitation (64.68 mm/year). The estimated site-scale annual dew yield (15.40 mm/year) was slightly less than the measured value (15.82 mm/year). The simulation results showed that the model performed better in summer and autumn, while there was some underestimation in spring and winter.

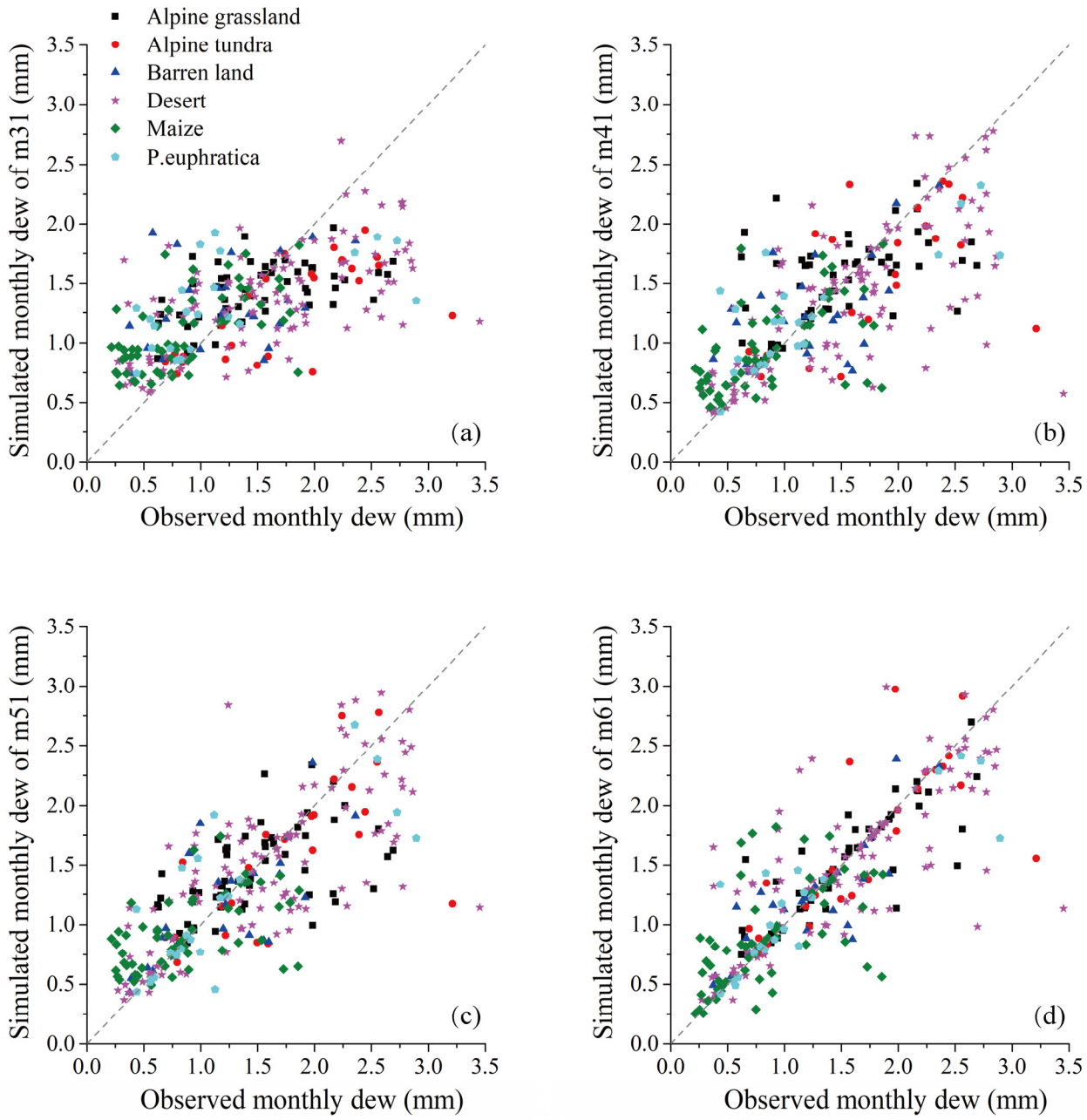

Figure 5. *Cont.*

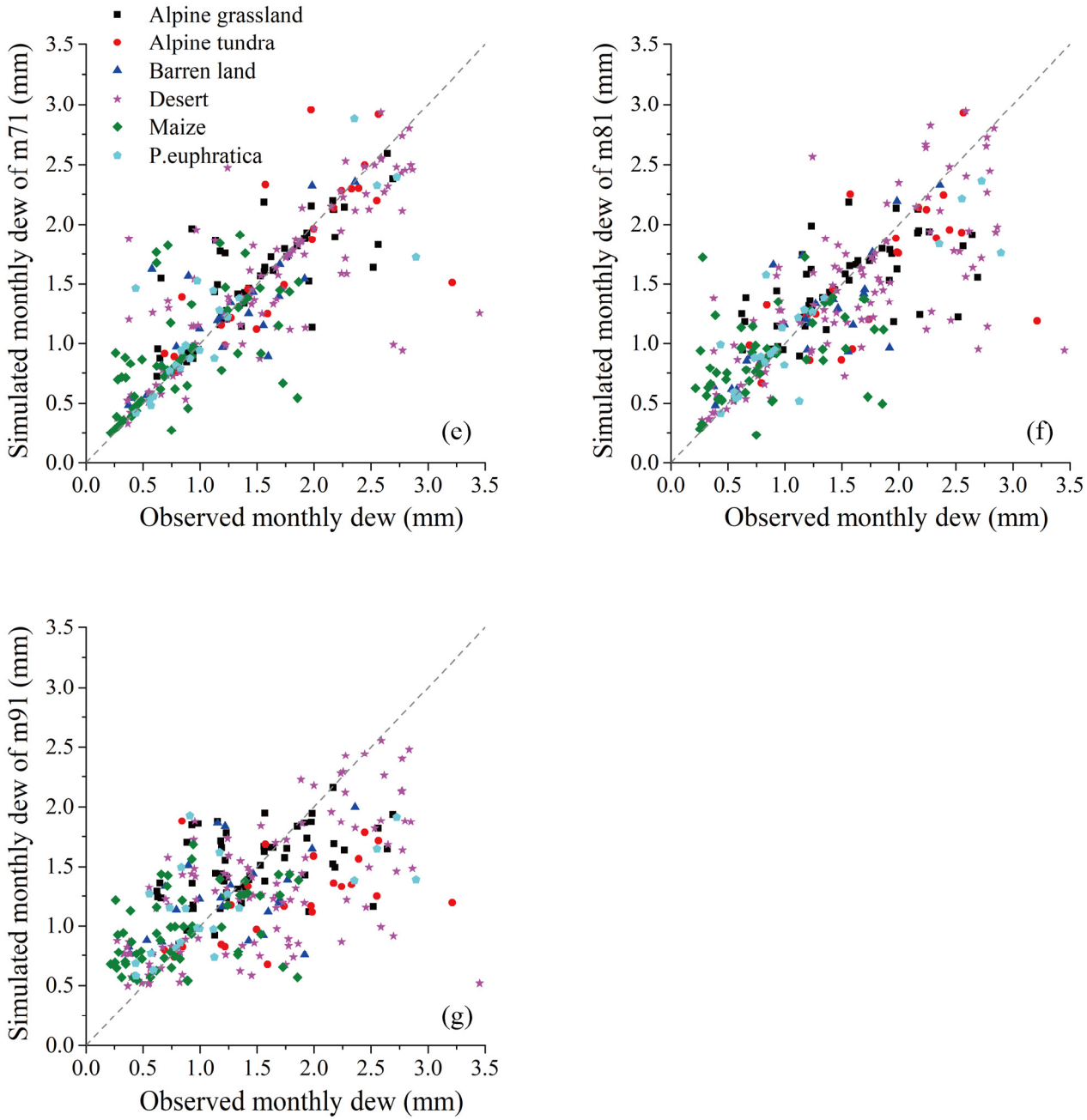

Figure 5. The scatter plots of the simulation results under different numbers of variables: (**a**–**g**) 3–9 variables, respectively.

3.3. Watershed-Scale Simulation

Using the chosen model, m62 (see Section 3.2), we calculated the monthly dew yield in the HRB. The basin-wide and upper and midstream monthly scale dew yields, respectively, for 2013–2017, are given in Figure 8. It can be seen that overall the dew yields were in the following order: downstream > upstream > midstream, from highest to lowest. In the upper reaches, there was a clear case of a sudden decrease in dew in July. In the midstream, there was no significant summer decrease, but the maximum did not exceed 1.5 mm/mon. The downstream area accounts for a larger area, and the trend of dew changes was more consistent with the results of the whole region, where there was a slight decrease in dew in July. These patterns can be seen more clearly in the multi-year monthly averages (Figure 9).

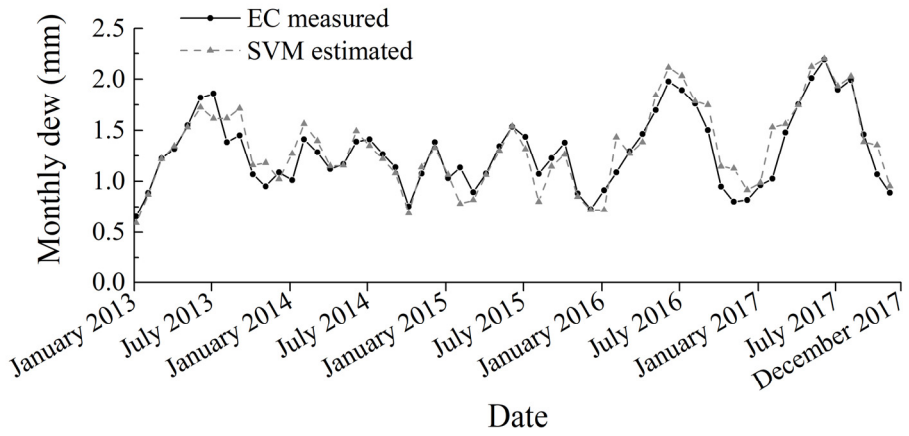

Figure 6. Site scale monthly dew SVM estimated and EC measured for 2013–2017.

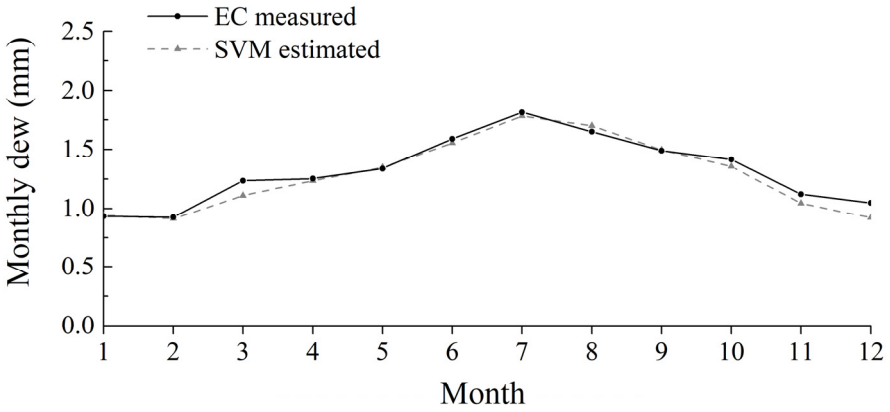

Figure 7. The average dew of each month estimated and EC measured for 2013–2017 SVM.

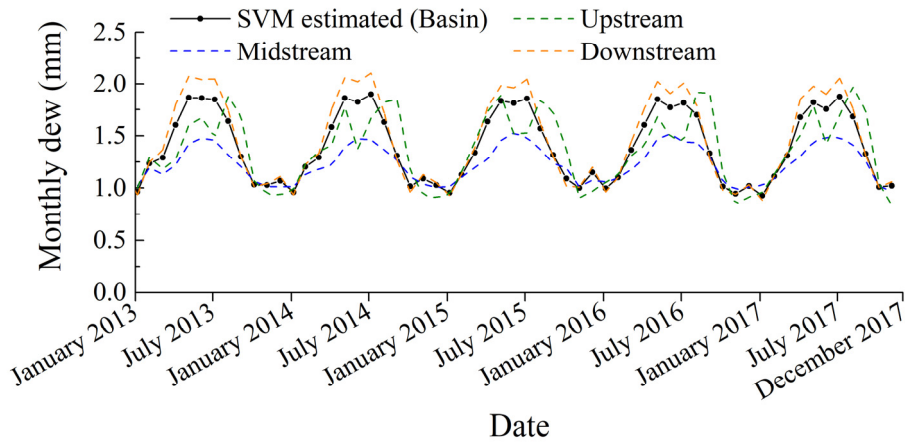

Figure 8. Basin-scale monthly dew yields estimated using SVM.

The distribution of the annual dew yield estimated by the m62 model in the HRB is shown in Figure 10. The annual dew yield across the HRB was found to range from 8.83 to 20.28 mm, with less dew in the upstream and midstream regions, along the river, and in the downstream tailrace. The lower reaches were found to have relatively high dew levels. The average annual dew in the HRB was 16.65 mm/year. High-altitude, riverine, and crop areas have relatively low amounts of dew, while large areas of bare land downstream have relatively high amounts of annual dew.

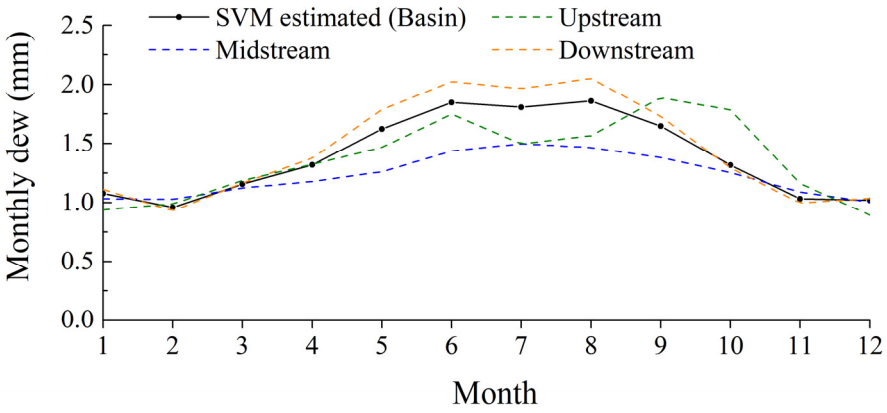

Figure 9. Basin-scale average dew of each month for 2013–2017 estimated using SVM.

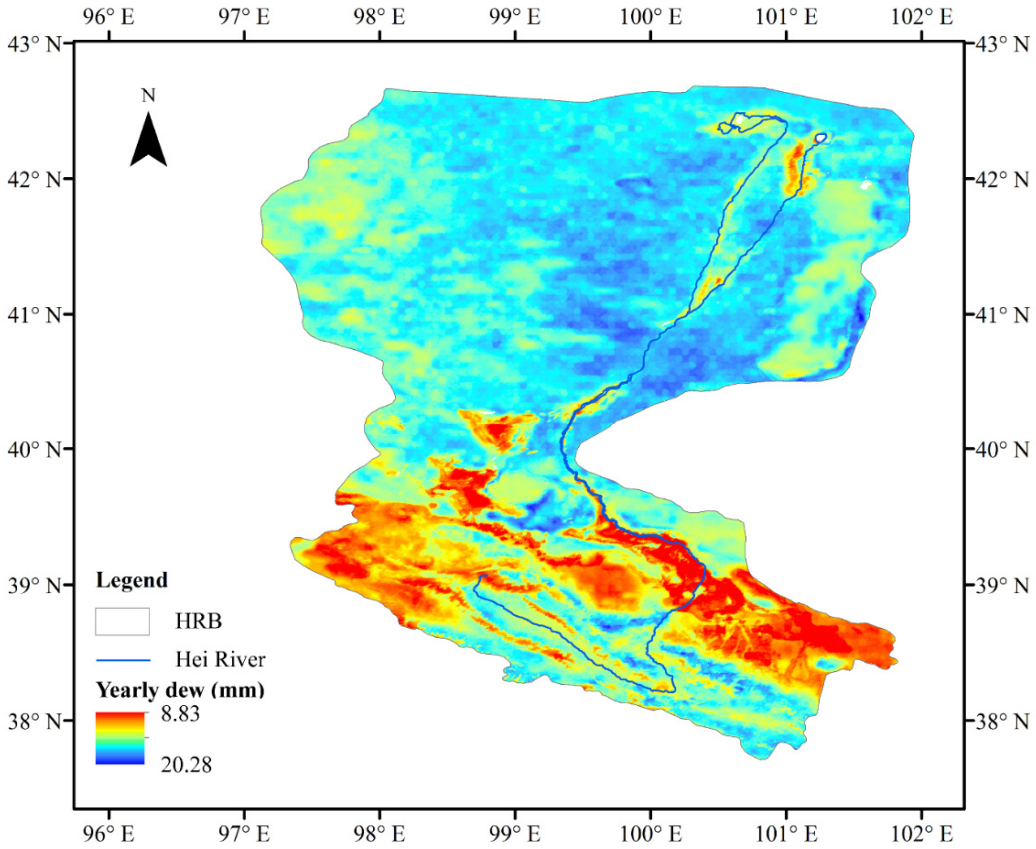

Figure 10. Basin-scale average amounts of dew per month for 2013–2017 estimated using the SVM model.

A histogram of the statistical distribution of the annual dew yields in the HRB was made, as shown in Figure 11. Most of the area of the HRB had an annual dew yield between 16 and 19 mm/year, accounting for 74.81%, with the highest percentage of the interval being 17~18 mm (39.4%), mainly in the downstream area.

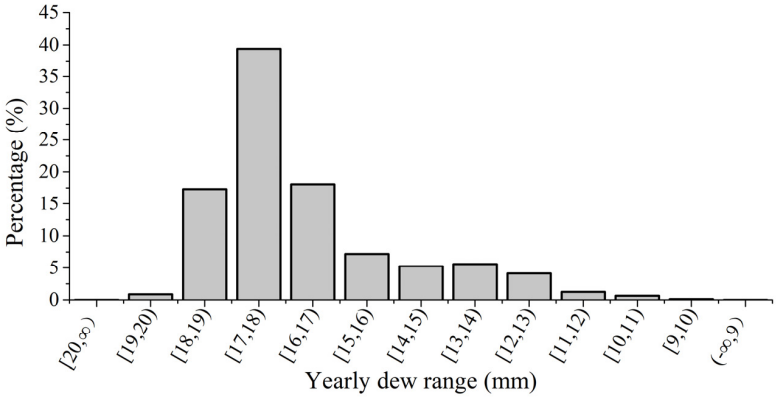

Figure 11. Histogram of the statistical distribution of the annual dew yields in the HRB.

4. Discussion

4.1. Variable Screening for Dew Simulation

Air temperature is an important factor influencing dew formation [39,42]. Surface temperature is one of the most important indirect indicators of soil water content and is widely used not only in reference to evapotranspiration estimation [25,53–55] but also in dew water estimation [20]. Therefore, we chose daytime and nighttime remote sensing land surface temperatures (LST_D and LST_N) as fixed variables, and other variables were combined with these as input variables for simulation.

As for the different surface band emissivities, bands 20, 22, and 23 are in the atmospheric window in the 3.5–4.2 μm medium-wavelength range, and bands 29–32 are in the 8–13 μm atmospheric window. Since the major absorber in bands 23 and 29 is water vapor, this could be the reason for their high relative contribution.

NDVI is an indicator that responds to the level of surface vegetation cover, and the leaf area index (LAI), which is similar to NDVI, has been used in the simulation of dew [28]. The effect of vegetation cover on dew reflects on shading, which is usually caused by surrounding objects such as plants, which may delay the condensation progress [56]. Specifically, the density and height of the canopy affects dew formation [57].

There are also some other studies regarding the effects of dew and other sensing data, such as visible, near-infrared, and thermal infrared sensors [58]; active microwave sensors [59]; and passive microwave sensors [41]. Using other band combinations or satellite products in the future may improve the fitting results somewhat, and the required factors may change for the non-arid sub-surfaces.

4.2. Distribution Characteristics of Dew in the HRB

The seasonal variation in dew yield was found to vary among the upper, middle, and lower reaches of the HRB. The dew yield may decrease a little in the summer months upstream and downstream (Figure 9). This phenomenon occurs in the Mu Us desert dominated by a mixture of deciduous shrub species [22], the Gurbantunggut Desert dominated by biological soil crusts [60] and the Badain Jaran Desert dominated by *H. ammodendron* [42], both in Northwest China. Diurnal temperature differences and water vapor supply are thought to be responsible for the differences between the dew yields in the wet and dry seasons [60,61]. Precipitation also affects the amount of dew by increasing soil moisture and thus reducing the water vapor adsorption capacity of the soil [62]. More summer precipitation in the upper reaches [63] may be the reason for the significant reduction of summer dew in this area compared to the lower reaches.

4.3. Contribution of Dew to Water Balance

Currently, dewfall is barely considered in water balance studies because the amounts are assumed to be very small. The annual precipitation and evaporation in the HRB range from 30~550 mm/year and 50~1000 mm/year, respectively, and evaporation is higher than

precipitation in the midstream and downstream areas [64]. The ratios of the annual dew yield to precipitation (https://www.resdc.cn/Default.aspx, accessed on 1 June 2021) and to evapotranspiration in the HRB yields, which were calculated using the GLDAS data product with the REDREW model [65] (unpublished results), are shown in Figure 12. Dew was found to account for 2.12~66.88% of precipitation and 1.02~55.11% of evapotranspiration in the HRB. Higher ratios were found in the downstream region. Rivers and irrigated areas had a smaller ratio due to high evaporation. In general, dew is a key element of the regional water balance.

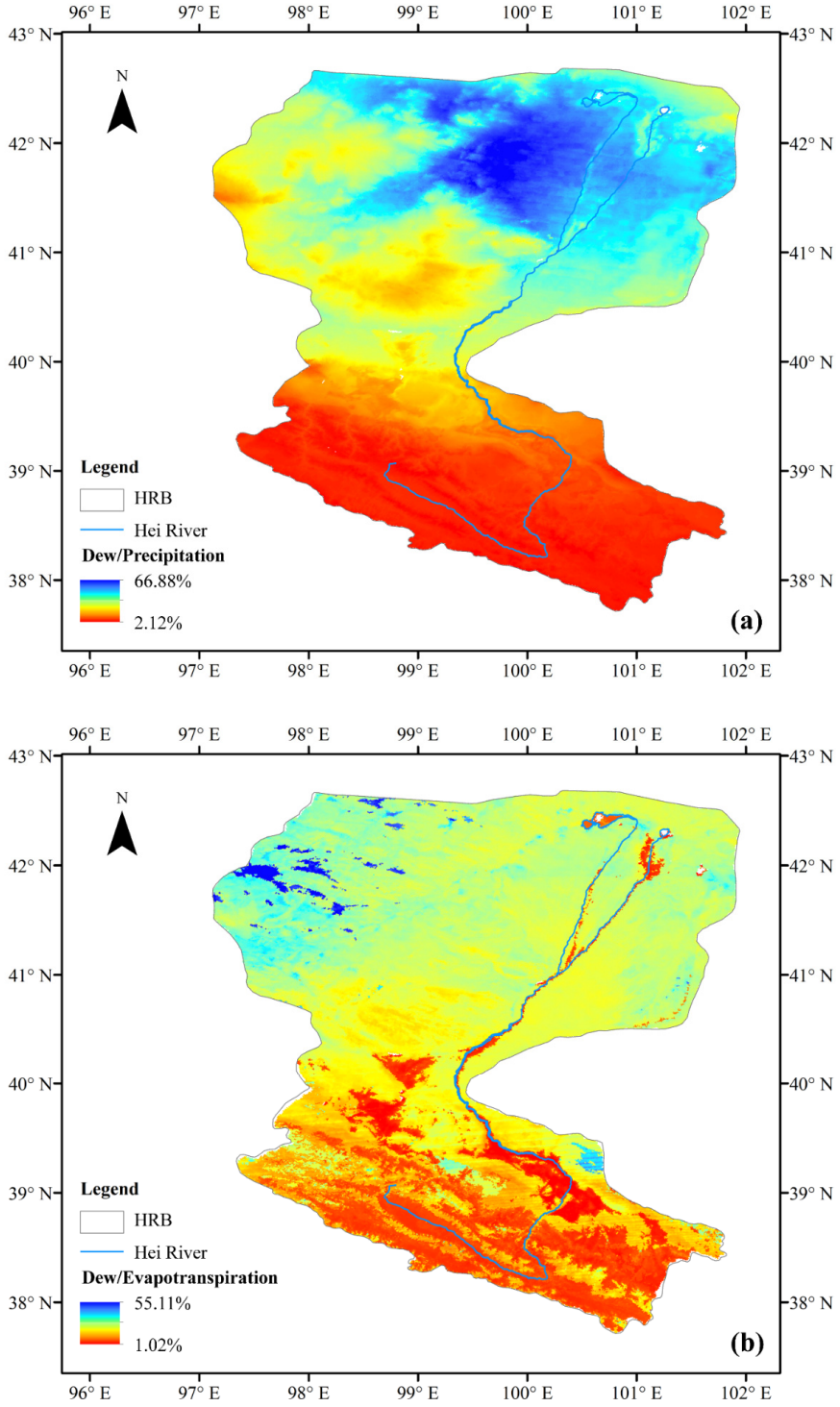

Figure 12. The ratio of annual dew to precipitation (**a**) and to evapotranspiration (**b**) in the HRB.

Many studies in arid and semiarid zones have shown the non-negligible character of the dew [21,61]. For example, in a closed desert valley in northeastern Nevada, USA, where precipitation is the only source of water, the cumulative amount of evapotranspiration (160 mm) during the water year 1993–1994 was greater than that of precipitation (131 mm), with dew contributing about 14 mm to the annual water balance [8]. During 2016, in a desert station in the HRB with no irrigation and no surface water replenishment channels, the dew amount (14.82 mm/year) filled the gap between precipitation (36.1 mm/year) and evapotranspiration (51.42 mm/year) [9]. In irrigated areas taking irrigation water into account, there is still a deficit that dew water can fill [10]. Under long-term observation, dew was found to reduce a deficit of 19~78 mm considerably, to between two and 41 mm, playing a more important role in dry years [61].

4.4. Model Applications in Northwest China

The m62 model was applied to Northwest China, and the amount of dew was estimated from 2011 to 2020 using remote sensing data. The annual-scale dew variation in several important northwestern watersheds is shown in Figure 13. All the basins showed significantly ($p < 0.05$) increasing trends in the annual dew yield to varying degrees, with similar increasing trends in precipitation [66].

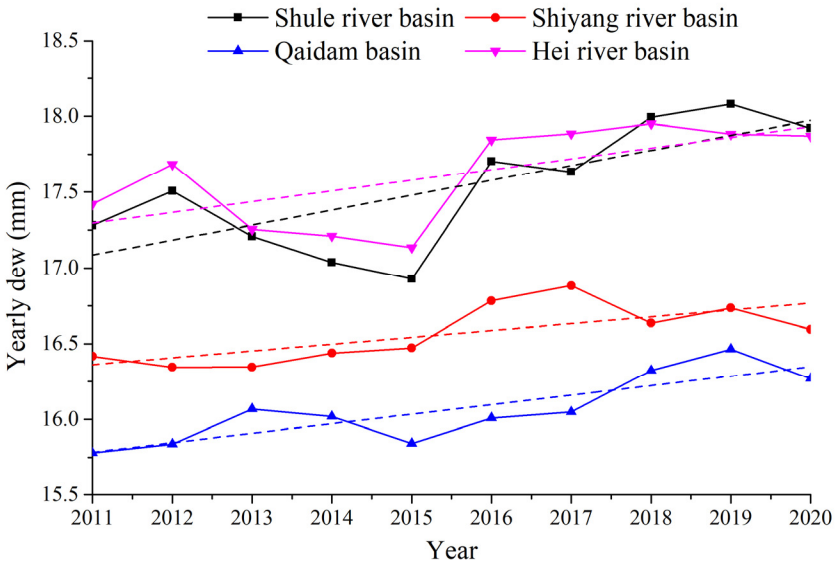

Figure 13. Annual dew variation in four typical basins in Northwest China (2011–2020), with the dashed line as the fitted line ($p < 0.05$).

The multi-year average northwest regional dew distribution is shown in Figure 14. The low-value areas in the HRB, Shiyang River Basin, and Shule River Basin are mainly agricultural land. Research in the Taklimakan Desert, China (N40.4572°, E87.8575°), using the open-path eddy covariance system observation method, showed that the average dewfall amount during the summer half-year (June–October 2011) was 17.2 mm [21]. This point shows a multi-year average dew amount of 18.32 mm/year in the simulation results of our model. Since the precipitation in this area is mainly concentrated in summer, and since dew itself is less abundant in spring and winter, we can assume that the model simulation results are like the actual measurements. Research in Shapotou Desert, China (N37.45°, E104.95°), using closed- or open-bottom cylindrical PVC containers under different cover types, showed an average dew yield of 12.15 mm in a one-year period (September 2013–August 2014) [56], which is similar to our model simulation result of 14.74 mm.

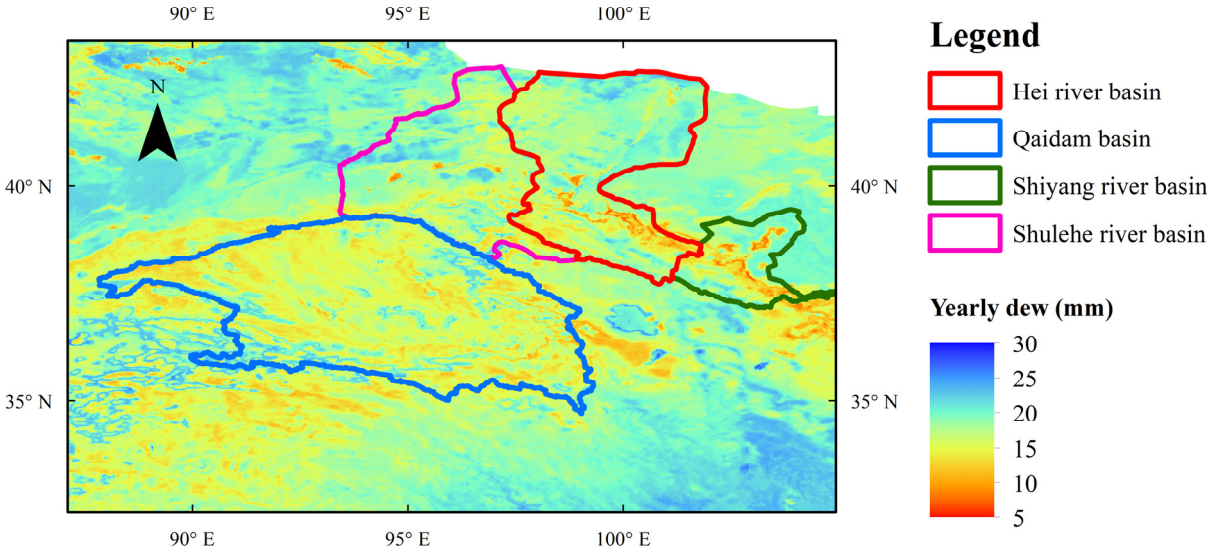

Figure 14. Average annual condensation water distribution from 2011 to 2020 in Northwest China.

5. Conclusions

This study used the SVM model, LST and NDVI remote sensing data, and different numbers of combinations of surface emissivity in bands 20, 22, 23, 29, 31, and 32 to simulate the monthly scale dew under different underlying surface conditions in arid areas ($p < 0.05$). Using the five-fold cross-validation method, when the combination of LST_D, LST_N, NDVI, $Emis_{22}$, $Emis_{31}$, and $Emis_{32}$ was used (m62), the overall performance of the model was better, and the CCs of the training set and test set reached 0.88 and 0.61 respectively.

By applying the best performing model (m62) to the HRB, we obtained the dew distribution from the remote sensing data. The highest dew amounts were found in the lower reaches. In the upper reaches, there was a clear double-peak phenomenon of the spring and autumn dew amounts. The annual dew yield was found to range from 8.83 to 20.28 mm/year throughout the region, accounting for 2.12~66.88% of the total precipitation in the same grid, with 74.81% of the area having an annual dew amount of 16 to 19 mm/year, making dew an integral part of the water balance of the region. The model was also applied to Northwest China, where the average multi-year dew yield from 2011 to 2020 is about five to 30 mm/year. Several important northwest basins showed a trend of increasing dew yield.

In summary, remote sensing data can be used to simulate the amount of dew under different underlying surface conditions in arid and semiarid areas. As a non-negligible part of the water cycle, the use of remote sensing to estimate dew can provide better support for future water resource calculations and analysis.

Author Contributions: Conceptualization, Y.S., Z.W. and Z.Z.; Data curation, Y.S. and Z.Z.; Formal analysis, Y.S. and Z.Z.; Funding acquisition, Z.W.; Methodology, Y.S. and Z.W.; Project administration, Z.W.; Software, Y.S. and Z.Z.; Supervision, Z.W. and S.R.F.; Validation, Y.S.; Visualization, Y.S.; Writing—original draft, Y.S.; Writing—review & editing, Y.S., Z.W. and S.R.F. All authors have read and agreed to the published version of the manuscript.

Funding: This research is funded by National Key R&D Program of China, Grant No. 2022YFE0101100, 2021YFD1900600 and 2021YFC3201204.

Conflicts of Interest: The authors declare no conflict of interest.

References

1. Agam, N.; Berliner, P.R. Dew formation and water vapor adsorption in semi-arid environments—A review. *J. Arid. Environ.* **2006**, *65*, 572–590. [CrossRef]
2. Wallin, J.R. Agrometeorological aspects of dew. *Agric. Meteorol.* **1967**, *4*, 85–102. [CrossRef]
3. Nikolayev, V.S.; Beysens, D.; Gioda, A.; Milimouk, I.; Katiushin, E.; Morel, J.P. Water recovery from dew. *J. Hydrol.* **1996**, *182*, 19–35. [CrossRef]
4. McHugh, T.A.; Morrissey, E.M.; Reed, S.C.; Hungate, B.A.; Schwartz, E. Water from air: An overlooked source of moisture in arid and semiarid regions. *Sci. Rep.* **2015**, *5*, 6. [CrossRef] [PubMed]
5. Wang, L.X.; Kaseke, K.F.; Ravi, S.; Jiao, W.Z.; Mushi, R.; Shuuya, T.; Maggs-Kolling, G. Convergent vegetation fog and dew water use in the Namib Desert. *Ecohydrology* **2019**, *12*, 11. [CrossRef]
6. Kidron, G.J.; Herrnstadt, I.; Barzilay, E. The role of dew as a moisture source for sand microbiotic crusts in the Negev Desert, Israel. *J. Arid. Environ.* **2002**, *52*, 517–533. [CrossRef]
7. Guadarrama-Cetina, J.; Mongruel, A.; Medici, M.G.; Baquero, E.; Parker, A.R.; Milimouk-Melnytchuk, I.; Gonzalez-Vinas, W.; Beysens, D. Dew condensation on desert beetle skin. *Eur. Phys. J. E* **2014**, *37*, 6. [CrossRef]
8. Malek, E.; McCurdy, G.; Giles, B. Dew contribution to the annual water balances in semi-arid desert valleys. *J. Arid. Environ.* **1999**, *42*, 71–80. [CrossRef]
9. Wang, Z.; Zhang, Z.; Suo, Y. A new water balance equation introducing dew amount in arid area. *J. Hydraul. Eng.* **2019**, *50*, 710–720.
10. Liu, X.Y.; Xu, J.Z.; Yang, S.H.; Zhang, J.G.; Wang, Y.J. Vapor Condensation in Rice Fields and Its Contribution to Crop Evapotranspiration in the Subtropical Monsoon Climate of China. *J. Hydrometeorol.* **2018**, *19*, 1043–1057. [CrossRef]
11. Beysens, D. Estimating dew yield worldwide from a few meteo data. *Atmos. Res.* **2016**, *167*, 146–155. [CrossRef]
12. Nilsson, T.M.J.; Vargas, W.E.; Niklasson, G.A.; Granqvist, C.G. Condensation of water by radiative cooling. *Renew. Energy* **1994**, *5*, 310–317. [CrossRef]
13. Jacobs, A.F.G.; Heusinkveld, B.G.; Berkowicz, S.M. Passive dew collection in a grassland area, The Netherlands. *Atmos. Res.* **2008**, *87*, 377–385. [CrossRef]
14. Heusinkveld, B.G.; Berkowicz, S.M.; Jacobs, A.F.G.; Holtslag, A.A.M.; Hillen, W. An automated microlysimeter to study dew formation and evaporation in arid and semiarid regions. *J. Hydrometeorol.* **2006**, *7*, 825–832. [CrossRef]
15. Hiltner, E. Der Tau und seine Bedeutung für den Pflanzenbau. *Wiss. Arch. Landw.* **1930**, *3*, 1–70.
16. Kidron, G.J. A simple weighing method for dew and fog measurements. *Weather* **1998**, *53*, 428–433. [CrossRef]
17. Beysens, D.; Milimouk, I.; Nikolayev, V.; Muselli, M.; Marcillat, J. Using radiative cooling to condense atmospheric vapor: A study to improve water yield. *J. Hydrol.* **2003**, *276*, 1–11. [CrossRef]
18. Kidron, G.J.; Kronenfeld, R. Microlysimeters overestimate the amount of non-rainfall water—An experimental approach. *Catena* **2020**, *194*, 104691. [CrossRef]
19. Madeira, A.C.; Kim, K.S.; Taylor, S.E.; Gleason, M.L. A simple cloud-based energy balance model to estimate dew. *Agric. For. Meteorol.* **2002**, *111*, 55–63. [CrossRef]
20. Groh, J.; Slawitsch, V.; Herndl, M.; Graf, A.; Vereecken, H.; Putz, T. Determining dew and hoar frost formation for a low mountain range and alpine grassland site by weighable lysimeter. *J. Hydrol.* **2018**, *563*, 372–381. [CrossRef]
21. Hao, X.M.; Li, C.; Guo, B.; Ma, J.X.; Ayup, M.; Chen, Z.S. Dew formation and its long-term trend in a desert riparian forest ecosystem on the eastern edge of the Taklimakan Desert in China. *J. Hydrol.* **2012**, *472*, 90–98. [CrossRef]
22. Guo, X.; Zha, T.; Jia, X.; Wu, B.; Feng, W.; Xie, J.; Gong, J.; Zhang, Y.; Peltola, H. Dynamics of dew in a cold desert-shrub ecosystem and its abiotic controls. *Atmosphere* **2016**, *7*, 32. [CrossRef]
23. Baldocchi, D.; Falge, E.; Gu, L.; Olson, R.; Hollinger, D.; Running, S.; Anthoni, P.; Bernhofer, C.; Davis, K.; Evans, R.; et al. FLUXNET: A New Tool to Study the Temporal and Spatial Variability of Ecosystem–Scale Carbon Dioxide, Water Vapor, and Energy Flux Densities. *Bull. Am. Meteorol. Soc.* **2001**, *82*, 2415–2434. [CrossRef]
24. Moro, M.J.; Were, A.; Villagarcia, L.; Canton, Y.; Domingo, F. Dew measurement by Eddy covariance and wetness sensor in a semiarid ecosystem of SE Spain. *J. Hydrol.* **2007**, *335*, 295–302. [CrossRef]
25. Zhang, Z.; Gong, Y.; Wang, Z. Accessible remote sensing data based reference evapotranspiration estimation modelling. *Agric. Water Manag.* **2018**, *210*, 59–69. [CrossRef]
26. Dorigo, W.; Wagner, W.; Albergel, C.; Albrecht, F.; Balsamo, G.; Brocca, L.; Chung, D.; Ertl, M.; Forkel, M.; Gruber, A.; et al. ESA CCI Soil Moisture for improved Earth system understanding: State-of-the art and future directions. *Remote Sens. Environ.* **2017**, *203*, 185–215. [CrossRef]
27. Hsu, K.L.; Gao, X.G.; Sorooshian, S.; Gupta, H.V. Precipitation estimation from remotely sensed information using artificial neural networks. *J. Appl. Meteorol.* **1997**, *36*, 1176–1190. [CrossRef]
28. Cosh, M.H.; Kabela, E.D.; Hornbuckle, B.; Gleason, M.L.; Jackson, T.J.; Prueger, J.H. Observations of dew amount using in situ and satellite measurements in an agricultural landscape. *Agric. For. Meteorol.* **2009**, *149*, 1082–1086. [CrossRef]
29. Vuollekoski, H.; Vogt, M.; Sinclair, V.A.; Duplissy, J.; Jarvinen, H.; Kyro, E.M.; Makkonen, R.; Petaja, T.; Prisle, N.L.; Raisanen, P.; et al. Estimates of global dew collection potential on artificial surfaces. *Hydrol. Earth Syst. Sci.* **2015**, *19*, 601–613. [CrossRef]
30. Shen, C.P. A transdisciplinary review of deep learning research and its relevance for water resources scientists. *Water Resour. Res.* **2018**, *54*, 8558–8593. [CrossRef]

31. Shalev-Shwartz, S.; Singer, Y.; Srebro, N.; Cotter, A. Pegasos: Primal estimated sub-gradient solver for SVM. *Math. Program.* **2011**, *127*, 3–30. [CrossRef]
32. Chang, C.-C.; Lin, C.-J. LIBSVM: A Library for Support Vector Machines. *Acm Trans. Intell. Syst. Technol.* **2011**, *2*, 3. [CrossRef]
33. Qiu, L.H.; Peng, D.Z.; Xu, Z.X.; Liu, W.F. Identification of the impacts of climate changes and human activities on runoff in the upper and middle reaches of the Heihe River basin, China. *J. Water Clim. Chang.* **2016**, *7*, 251–262. [CrossRef]
34. Song, L.S.; Liu, S.M.; Kustas, W.P.; Nieto, H.; Sun, L.; Xu, Z.W.; Skaggs, T.H.; Yang, Y.; Ma, M.G.; Xu, T.R.; et al. Monitoring and validating spatially and temporally continuous daily evaporation and transpiration at river basin scale. *Remote Sens. Environ.* **2018**, *219*, 72–88. [CrossRef]
35. Li, X.; Liu, S.; Ma, M.; Xiao, Q.; Liu, Q.; Jin, R.; Che, T.; Wang, W.; Qi, Y.; Li, H.; et al. HiWATER:An Integrated Remote Sensing Experiment on Hydrological and Ecological Processes in the Heihe River Basin. *Adv. Earth Sci.* **2012**, *27*, 481–498.
36. Liu, S.M.; Li, X.; Xu, Z.W.; Che, T.; Xiao, Q.; Ma, M.G.; Liu, Q.H.; Jin, R.; Guo, J.W.; Wang, L.X.; et al. The Heihe Integrated Observatory Network: A Basin-Scale Land Surface Processes Observatory in China. *Vadose Zone J.* **2018**, *17*, 21. [CrossRef]
37. Liu, S.M.; Xu, Z.W.; Wang, W.Z.; Jia, Z.Z.; Zhu, M.J.; Bai, J.; Wang, J.M. A comparison of eddy-covariance and large aperture scintillometer measurements with respect to the energy balance closure problem. *Hydrol. Earth Syst. Sci.* **2011**, *15*, 1291–1306. [CrossRef]
38. Xu, Z.; Liu, S.; Li, X.; Shi, S.; Wang, J.; Zhu, Z.; Xu, T.; Wang, W.; Ma, M. Intercomparison of surface energy flux measurement systems used during the HiWATER-MUSOEXE. *J. Geophys. Res. Atmos.* **2013**, *118*, 13–140. [CrossRef]
39. Fang, J. Variability in condensation water and its determinants in arid regions of north-western China. *Ecohydrology* **2020**, *13*, e2226. [CrossRef]
40. Meng, Y.; Wen, X.F. Characteristics of dew events in an arid artificial oasis cropland and a sub-humid cropland in China. *J. Arid Land* **2016**, *8*, 399–408. [CrossRef]
41. De Jeu, R.; Heusinkveld, B.; Vugts, H.; Holmes, T.; Owe, M. Remote sensing techniques to measure dew: The detection of canopy water with an L-band passive microwave radiometer and a spectral reflectance sensor. In Proceedings of the Conference on Remote Sensing for Agriculture, Ecosystems and Hydrology VI, Maspalomas, Spain, 14–16 September 2004; pp. 225–235.
42. Zhuang, Y.; Zhao, W. Dew formation and its variation in Haloxylon ammodendron plantations at the edge of a desert oasis, northwestern China. *Agric. For. Meteorol.* **2017**, *247*, 541–550. [CrossRef]
43. Vapnik, V. *The Nature of Statistical Learning Theory*; Springer: Berlin/Heidelberg, Germany, 1995.
44. Tehrany, M.S.; Pradhan, B.; Jebur, M.N. Flood susceptibility mapping using a novel ensemble weights-of-evidence and support vector machine models in GIS. *J. Hydrol.* **2014**, *512*, 332–343. [CrossRef]
45. Gevrey, M.; Dimopoulos, I.; Lek, S. Review and comparison of methods to study the contribution of variables in artificial neural network models. *Ecol. Model.* **2003**, *160*, 249–264. [CrossRef]
46. Olden, J.D.; Jackson, D.A. Illuminating the "black box": A randomization approach for understanding variable contributions in artificial neural networks. *Ecol. Model.* **2002**, *154*, 135–150. [CrossRef]
47. Garson, G.D. Interpreting neural-network connection strengths. *AI Expert* **1991**, *6*, 47–51.
48. *MATLAB and Deep Learning Toolbox, R2021b*; The MathWorks, Inc.: Natick, MA, USA, 2021.
49. Beysens, D.; Mongruel, A.; Acker, K. Urban dew and rain in Paris, France: Occurrence and physico-chemical characteristics. *Atmos. Res.* **2017**, *189*, 152–161. [CrossRef]
50. Tuure, J.; Korpela, A.; Hautala, M.; Hakojärvi, M.; Mikkola, H.; Räsänen, M.; Duplissy, J.; Pellikka, P.; Petäjä, T.; Kulmala, M.; et al. Comparison of surface foil materials and dew collectors location in an arid area: A one-year field experiment in Kenya. *Agric. For. Meteorol.* **2019**, *276–277*, 107613. [CrossRef]
51. Taylor, K.E. Summarizing multiple aspects of model performance in a single diagram. *J. Geophys. Res. Atmos.* **2001**, *106*, 7183–7192. [CrossRef]
52. Dimitriadou, S.; Nikolakopoulos, K.G. Multiple Linear Regression Models with Limited Data for the Prediction of Reference Evapotranspiration of the Peloponnese, Greece. *Hydrology* **2022**, *9*, 124. [CrossRef]
53. Ferreira, L.B.; da Cunha, F.F.; Fernandes, E.I. Exploring machine learning and multi-task learning to estimate meteorological data and reference evapotranspiration across Brazil. *Agric. Water Manag.* **2022**, *259*, 107281. [CrossRef]
54. Dimitriadou, S.; Nikolakopoulos, K.G. Artificial Neural Networks for the Prediction of the Reference Evapotranspiration of the Peloponnese Peninsula, Greece. *Water* **2022**, *14*, 2027. [CrossRef]
55. Zakeri, M.S.; Mousavi, S.F.; Farzin, S.; Sanikhani, H. Modeling of Reference Crop Evapotranspiration in Wet and Dry Climates Using Data-Mining Methods and Empirical Equations. *J. Soft Comput. Civ. Eng.* **2022**, *6*, 1–28. [CrossRef]
56. Pan, Y.X.; Wang, X.P.; Zhang, Y.F.; Hu, R. Dew formation characteristics at annual and daily scale in xerophyte shrub plantations at Southeast margin of Tengger desert, Northern China. *Ecohydrology* **2018**, *11*, 13. [CrossRef]
57. Pan, Y.X.; Wang, X.P.; Zhang, Y.F. Dew formation characteristics in a revegetation-stabilized desert ecosystem in Shapotou area, Northern China. *J. Hydrol.* **2010**, *387*, 265–272. [CrossRef]
58. Pinter, P.J. Effect of dew on canopy reflectance and temperature. *Remote Sens. Environ.* **1986**, *19*, 187–205. [CrossRef]
59. Lin, B.; Minnis, P. Temporal variations of land surface microwave emissivities over the atmospheric radiation measurement program southern great plains site. *J. Appl. Meteorol.* **2000**, *39*, 1103–1116. [CrossRef]
60. Jia, Z.; Zhao, Z.; Zhang, Q.; Wu, W. Dew yield and its influencing factors at the western edge of Gurbantunggut desert, China. *Water* **2019**, *11*, 733. [CrossRef]

61. Aguirre-Gutiérrez, C.A.; Holwerda, F.; Goldsmith, G.R.; Delgado, J.; Yepez, E.; Carbajal, N.; Escoto-Rodríguez, M.; Arredondo, J.T. The importance of dew in the water balance of a continental semiarid grassland. *J. Arid. Environ.* **2019**, *168*, 26–35. [CrossRef]
62. Zhang, Q.; Wang, S.; Wang, S.S.; Zhao, Y.D.; Wen, X.M. Influence factors and variation characteristics of water vapor absorption by soil in semi-arid region. *Sci China Earth Sci* **2016**, *59*, 2240–2251. [CrossRef]
63. Su, Y.; Zhao, C.; Wang, Y.; Ma, Z. Spatiotemporal variations of precipitation in China using surface gauge observations from 1961 to 2016. *Atmosphere* **2020**, *11*, 303. [CrossRef]
64. Xu, Z.W.; Liu, S.M.; Zhu, Z.L.; Zhou, J.; Shi, W.J.; Xu, T.R.; Yang, X.F.; Zhang, Y.; He, X.L. Exploring evapotranspiration changes in a typical endorheic basin through the integrated observatory network. *Agric. For. Meteorol.* **2020**, *290*, 108010. [CrossRef]
65. Feng, J.; Wang, Z. A satellite-based energy balance algorithm with reference dry and wet limits. *Int. J. Remote Sens.* **2013**, *34*, 2925–2946. [CrossRef]
66. Yang, T.; Ala, M.; Guan, D.; Wang, A. The Effects of Groundwater Depth on the Soil Evaporation in Horqin Sandy Land, China. *Chin. Geogr. Sci.* **2021**, *31*, 727–734. [CrossRef]